Biological Journal of the Linnean Society, 2023, **138**, 132–140. With 5 figures.

View from below: experimental manipulation of water surfaces to evaluate visual integrity of heron-like models through Snell's window

A. R. B. CORTESE[1] and T. E. REIMCHEN[1*]

[1]*Department of Biology, University of Victoria, PO Box 1700, Victoria, British Columbia, V8W 2Y2, Canada*

Received 10 August 2022; revised 7 October 2022; accepted for publication 18 October 2022

The water–air interface is a globally widespread habitat for interactions between prey and predators. We experimentally manipulated water surface conditions (flat, smooth waves, three levels of current-induced turbulence) and digitally quantified the visual integrity of above-surface models from a subsurface perspective. Progressive fragmentation was present in each of the models (upright heron, crouched heron, vertical block, horizontal block) with increased departure from flat surface conditions. Smooth directional waves produced multiple horizontal bands (shadows) that moved across the models while surface currents distorted the profile, including progressive disintegration of the models appearance into multiple fragments of different sizes. This fragmentation is caused by scattered surface irregularities interacting with waves and is accentuated at the broken periphery of the optical window, reducing recognition of the models. Unexpectedly, we found that bands and fragments emerging from different surface conditions resemble common frontal plumage patterns on some Ardeidae and shorebirds (Charadriiformes). While these natural plumages are widely recognized to reflect a diversity of adaptations, including camouflage in terrestrial habitats, we suggest that their resemblance to water surface-induced fragmentation might also reflect foraging adaptations of predators though the water–air interface.

ADDITIONAL KEYWORDS: Ardeidae – avian plumage – Charadriiformes – disruptive coloration – flicker-fusion – foraging behaviour – optical window – predator–prey – visual fragmentation

INTRODUCTION

Distinct from species interactions within aquatic or terrestrial habitats, interactions through the water–air interface involve an unusual visual geometry between prey and predator. From the perspective of a prey beneath a flat water surface, the entire above-surface hemisphere (horizon to horizon) is compressed into a 97° cone (Snell's window) due to the physics of light refraction (Lythgoe, 1979). This condition is exploited by some predatory fish hunting through this smooth interface (Dill, 1977; Temple *et al.*, 2010; Day *et al.*, 2016). An aerial or shoreline predator above the surface would be visible to subsurface prey viewed against the sky or terrestrial background within this narrow window. Apart from the progressive compression near the edge of the window (Horvath & Varju, 1995), the profile of a predator would be seen as relatively intact. However, waves and currents result in expansion and distortion of the optical window (Lynch, 2015), potentially obscuring predator profiles. Similarly, assessment of feeding in avian piscivores indicates reduced foraging success in windy conditions, possibly due to reduced detection of the subsurface prey (Dunn, 1973; Grubb, 1977; Bovino & Burtt, 1979; Taylor, 1983; Dodd & Colwell, 1996; McGowan *et al.*, 2002; Green & Leberg, 2005; Taylor & Taylor, 2005) although recent arctic studies on terns (Laridae) indicate increased success in turbulent waters (Lieber *et al.*, 2021).

Characterization of the optical window through disturbed water surfaces has received very little attention from ecologists, which is unexpected given that the wave-influenced water–air interface is such a globally distributed habitat. Extending from several recent field studies examining salmon evasive responses to predatory bears and predator models

*Corresponding author. E-mail: reimchen@uvic.ca

(Reimchen, 2000; Klinka & Reimchen, 2002, 2009; Reimchen *et al.*, 2021), we experimentally manipulate surface conditions and, using digital sub-surface imagery, quantify the fragmentation and temporal changes of above-surface models that resemble a large avian wader (Ardeidae). Our results indicate that non-breaking waves differ fundamentally from surface currents in their effects on the visual integrity of above-surface models and we consider whether this has relevance to frontal plumage differences among avian species using the water–air interface.

MATERIALS AND METHODS

The experimental protocol (Fig. 1A) (full details in Supporting Information, Methods S1), undertaken at the University of Victoria Aquatic Centre, involved an outdoor tank (155 cm length, 94 cm width, 63 cm depth) filled to a depth of 41 cm and with a predator-model placed at the end of the tank on two 45-cm 'legs' (0.5 cm circumference) such that the body was positioned 5 cm above the water surface. A digital video camera in a waterproof housing was positioned in the tank 33 cm under the water surface at an ~45° angle above the horizontal facing the model. All experiments were carried out at night with the model illuminated by a 60-W bulb at the opposite end of the tank and two 25-W LED lamps on each side positioned midway down the tank to minimize any shading on the models and to control for consistency within the background.

Four Styrofoam model configurations were used in the experiments: 1, a life-like model of a tall heron (TH) in an upright position (43 cm high, 14 cm wide, Fig. 1B); 2, a heron model in a crouched posture (CH) (18 cm high, 14 cm wide, Fig. 1C); 3, a tall rectangular block (TB) (63 cm × 15 cm); and 4, a 'crouched' rectangular block (CB) (15 cm × 63 cm), the latter two (Fig. 1D) being used to provide a more exaggerated spatial representation of model shapes. To facilitate image processing (see Supporting Information, Methods S2), each model was tightly wrapped in a red monotone polyester fabric to eliminate any shadow-producing folds on the model. Each pair (TH/CH, TB/CB) had an equal surface area to each other but different spatial configurations above the surface and within the optical window.

Water surface conditions were manipulated with two methods. To simulate surface waves, a Styrofoam block (94 × 25 × 8 cm) that spanned the width of the tank was placed on the surface of the water behind the field of view of the camera. The block was manually depressed (~2 cm) approximately five times per second causing regular movement of smooth, non-breaking surface waves along the length of the tank towards the

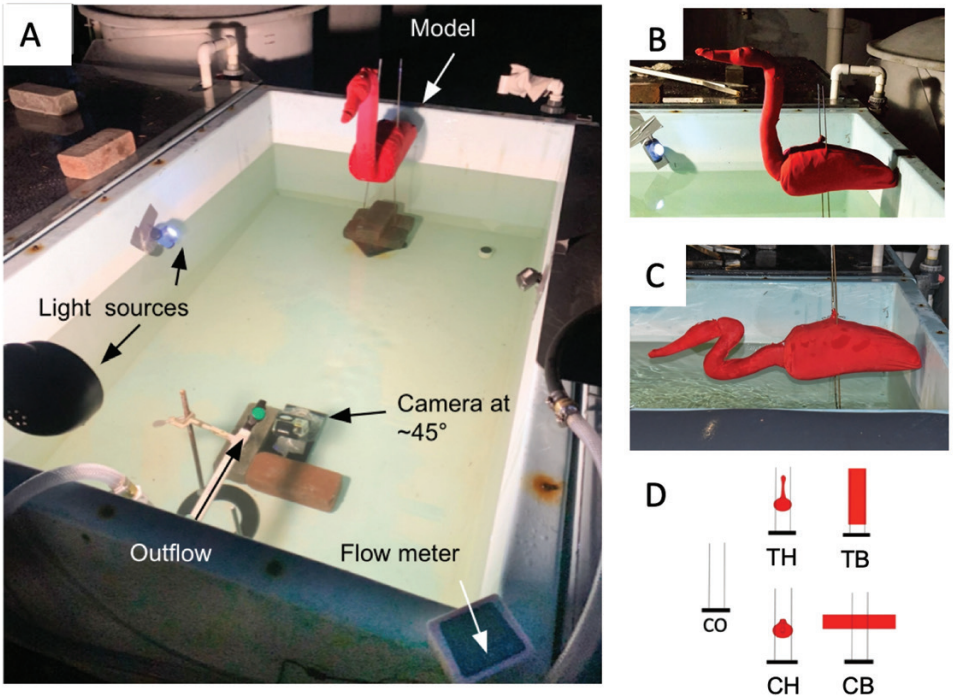

Figure 1. Experimental setup used to obtain underwater videos for image analysis. A, a large steel tank filled with water containing an underwater camera angled at ~45° towards the surface capturing each above-surface model; B and C, upright (B) and crouched (C) wading-bird models (TH/CH); D, representations of each of the four experimental models and the control (CO).

model (Fig. 2A) with occasional irregularities in the curvature of the wave. To produce current-like surface conditions, a PVC pipe (diameter = 1.3 cm) connected to a freshwater source was placed on the water surface 10 cm behind the camera to create surface flow in the tank. The flow rate was adjusted (Digital LCD Display water flow-meter) to produce four conditions: zero flow (flat), 2 L/min (low-flow), 4 L/min (medium flow) and 8 L/min (high flow). The different flows imparted repeatable characteristics to the surface, including small dynamic ripples at low flow (Fig 2B), an oscillating checkerboard of ripples across the entire surface at medium flow (Fig. 2C) and increased turbulence and directionality at high flow (Fig. 2D). The depth of the water in the tank was re-adjusted to 41 cm prior to each new trial.

Underwater video sequences (1920 × 1080 pixels, 30 fps) lasting 1 min were made of each model under the five surface conditions (flat, smooth waves, low flow, medium flow and high flow) on a SJ4000 CAM compact camera (see Supporting Information, Videos S2–S5). In video sequences made under flat surface conditions, 100 representative 1920 × 1080-pixel jpeg frames were retrieved for each model in which the border of Snell's window was unobscured. From each of the surface conditions, a 10-s video clip was selected from the complete sequence. Stop frame jpeg images were then obtained from these clips by retrieving an image every 0.1 s providing 100 image frames for each 10-s surface flow condition. For the wave conditions, stop frame images were extracted using a 5-s clip resulting in 50 frames. These sequential frames were collected for each model and surface combination and used for analyses of fragmentation and model areas. For details of the digital analyses, see Methods S2.

Using model areas obtained through image analyses, percentage expansion (> 0) or compression (< 0) values (change in model area) were calculated for all frame sets by subtracting flow-induced area values from that of each respective model area as obtained through a flat surface and compared (ANOVA). Differences in fragmentation (number of model patches in a frame) between model pairings were compared across all surface treatments and between model pairing using separate two-way ANOVA with *post hoc* comparisons (Tukey's HSD). Analyses of model fragmentation were performed as unbalanced designs to account for the differing number of frames within the wave condition which had 50 rather than 100 frames. Since raw data describing the number of patches in a frame as well as overall model area followed a non-normal

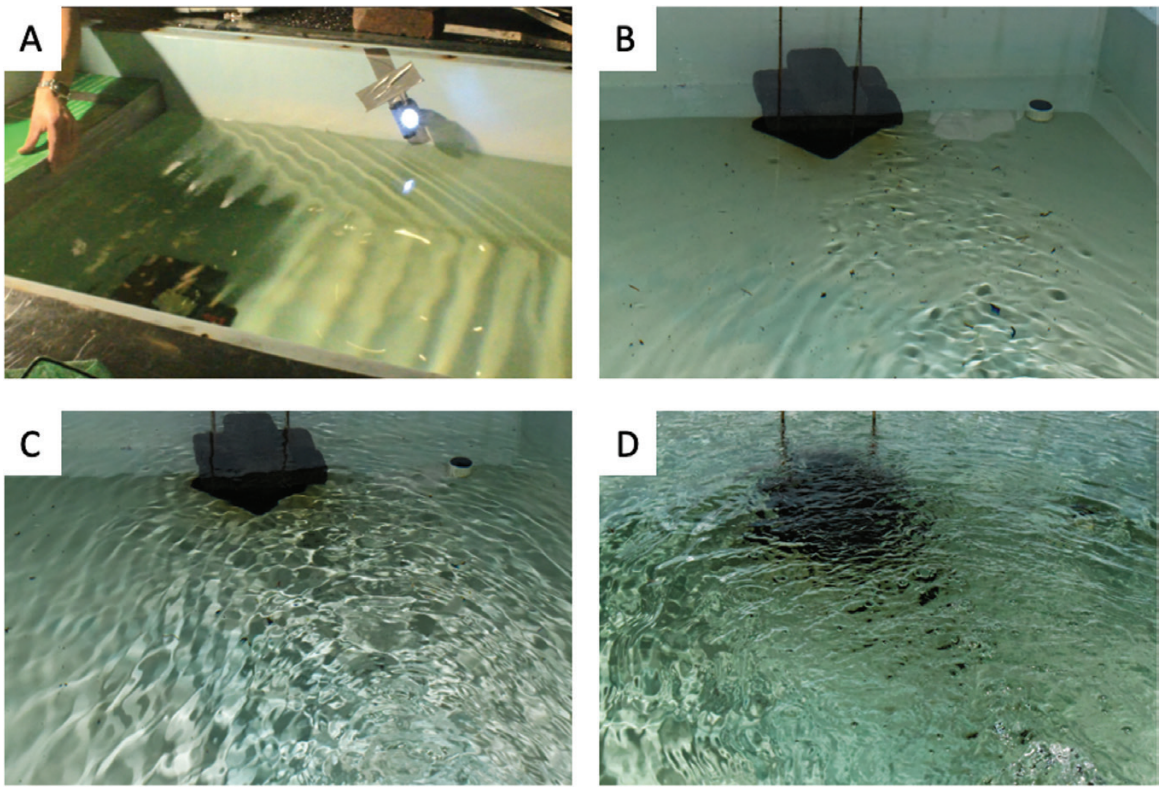

Figure 2. Visual representations of all experimentally manipulated surface conditions used for videography of models from the subsurface perspective. A, waves; B, low flow (2 L/min); C, medium flow (4 L/min); and D, high flow (8 L/min).

distribution, all data were log-transformed (ln) prior to analysis. Statistical analyses were performed using R 4.1.2 (R Core Team, 2022) with $P = 0.05$ indicating significance, and graphical data were created using the R-package 'ggplot2' (Wickham, 2016).

RESULTS

For each of the four models, increasing levels of surface disturbance resulted in an increased number of model fragments within the field of view compared to appearance through a flat surface (see Fig. 3). With smooth waves, the edges of the models remain relatively intact but the main bodies of the models become horizontally separated into fragments [mean ($\bar{X}$) = 2.7, range 1–12 among frames, Fig. 3.3]. With low flow, the edges of the models become distorted with minor fragmentation ($\bar{X}$ = 1.3, range 1–4 among frames, Fig. 3.4). With intermediate flow, fragmentation is more extensive ($\bar{X}$ = 4.2, range 1–11 among frames, Fig. 3.5). With high flow, fragmentation was most extensive ($\bar{X}$ = 16.5, range 4–33, Fig. 3.6) intruding into the interior of the models as well as occupying increasing proportions of the overall window (comparison among means, $F_{(3,1396)} = 1977$, $P < 0.001$).

The extent of fragmentation differed with respect to model type and position in the window for the same surface conditions (Fig. 4). The tall heron (TH) showed greater fragmentation than the crouched heron (CH) for the low and intermediate flows but not for the wave or high flow condition ($F_{(4,440)} = 13.2$, $P < 0.001$, Fig. 4A). However, the tall block (TB) had a lower number of fragments than the crouched block (CB) for waves, medium and high currents ($F_{(4,440)} = 24.0$, $P < 0.001$) despite being the same model size (Fig. 4B). This difference was associated with model orientation as TB extended much further into the centre of the optical window as compared with CB, which occurred along the edge of the window where fragmentation is more prevalent.

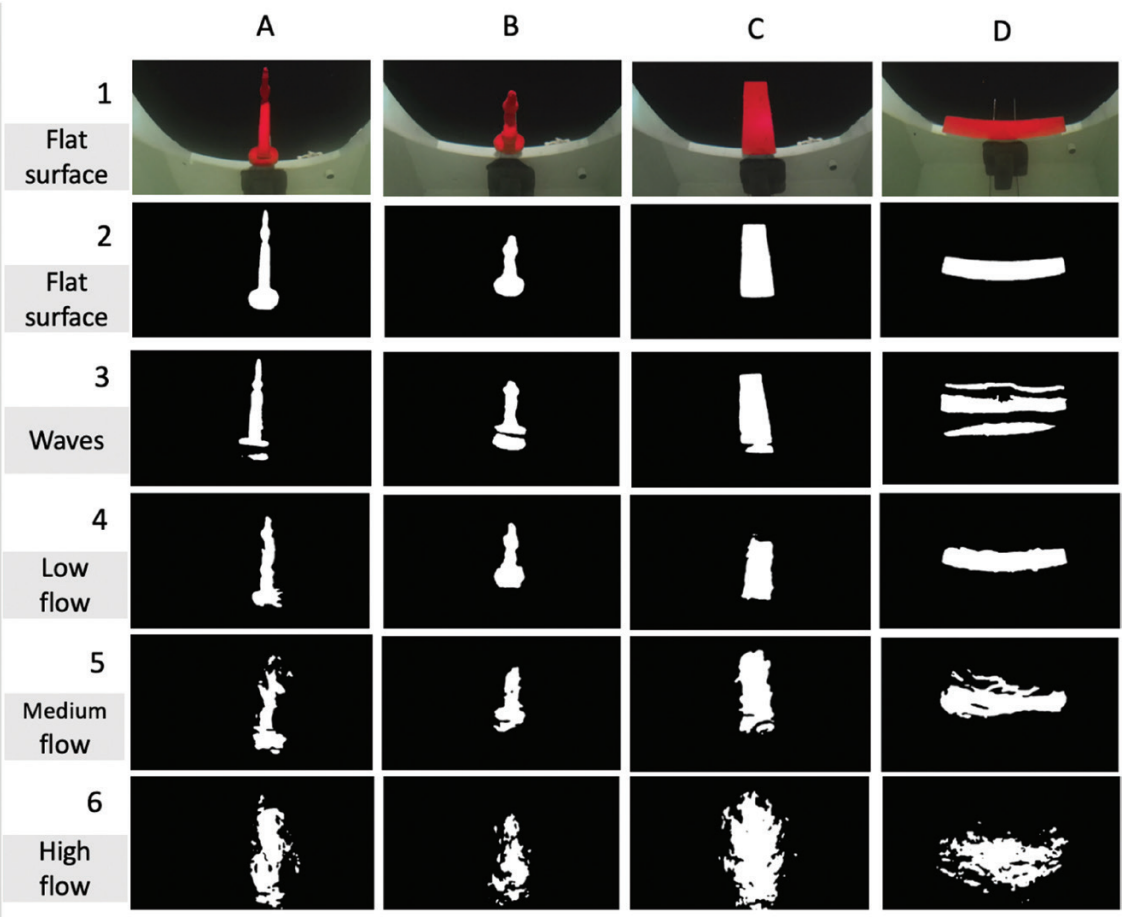

Figure 3. Model appearance for each surface condition imaged through Snell's window (A, upright heron model; B, crouched heron model; C, upright rectangular block; D, crouched rectangular block). 1, flat surface prior to image analysis; 2, flat surface following image analyses; 3, waves; 4, low flow; 5, medium flow; 6, high flow.

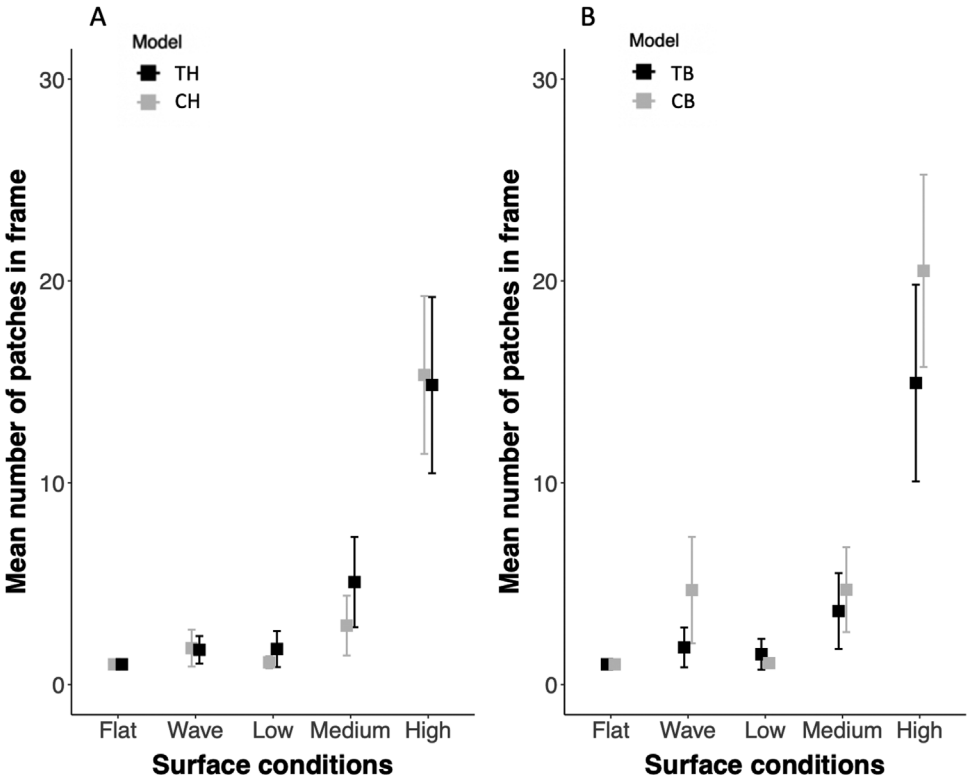

Figure 4. The mean number of model patches (±2 SD) (degree of model fragmentation) under five levels of surface treatments (flat, waves, low flow, medium flow, high flow). A, tall heron vs. crouched heron; B, tall block vs. crouched block.

Overall model area also varied with respect to both surface conditions and position in the window. Relative to a flat surface model area, there was compression (reduction of image area) in occasional frames in each of the four models during low flow conditions although an average area reduction occurred only in the tall heron (TH, 11.5% reduction) and in the tall block (TB, 20.6% reduction). In the medium surface flow, there was a mean area expansion across all four models (TH, 3.5%; CH, 7.8%; TB, 9.2%; CB, 20.9%). Under high flow surface conditions, compression in area was not observed on any individual frames and there was a consistent area increase in all models (TH, 78.6%; CH, 30.3%; TB, 103.4%; CB, 58.0%). All comparisons with model area for a flat-water surface were statistically informative (ANOVA, all $P < 0.001$; *Post hoc* Tukey: $P < 0.001$). We found that the number of fragments and total area of the models was highly correlated ($r = 0.73$) and thus restricted subsequent analyses primarily to fragmentation.

Visualization of sequential stop-frames indicates rapid (< 1 s) temporal shifts in model integrity in relation to surface conditions (see Supporting Information, Fig. S2 and Videos S2–S5). For the tall and crouched heron (TH and CH), in low flow and medium flow, overall shape becomes distorted between sequential frames but the focal model patch remains largely intact. At low flow over 10 s, the TH model area fluctuated from –26.7% to –0.2% reduction when compared to the original area through a flat surface while patches ranged from one to four. The CH model area fluctuated from –3.9% to +10.7% and patches from one to two. For increased flow, there was a progressive increase in area and number of fragments (medium flow: TH, Area: –17.4% to 20.4%, Fragments: 1–10; CH, Area: –9.9% to 24.9%, Fragments: 1–7; high flow: TB, Area: 45.0% to 113.4%, Fragments: 7–26; CB, Area: –15.7% to 69.2%, Fragments: 4–33).

DISCUSSION

We examined experimentally the integrity and spatial composition of various above-surface models visualized through Snell's window across diverse surface conditions. In summary, we found that waves and currents differed in their effect on model integrity, the former producing horizontal banding on the models and the latter producing increased distortion and fragmentation. Increasing total area of the model profiles was highly correlated with the extent of fragmentation ($r^2 = 0.54$, d.f. = 1798), and at the

highest flow in which the water surface was composed of multiple interacting concave and convex surfaces, the profile of the models was extensively fragmented.

Our experimental protocol has relevance to natural habitats. The flat-water surface that yields a 97° optical cone and full integrity of objects within the window is probably least representative in nature but could occur in habitats protected from winds or water flow, for example ponds and small lakes. Smooth waves, our second condition, are common in nature and resemble the slow directional movement of light wind-induced non-breaking waves onto shorelines. These smooth waves can also result directly from the forager in calm water, as small concentric waves are produced during leg or body movement (our personal observations); this will presumably alter the subsurface optical window in front of the waders. Low flow conditions are similar to those found on a slow-moving stream where eddies and substrate obstructions interact to produce an irregular surface. Medium and high current conditions resemble those of medium- to fast-flowing streams with turbulence and possibly wind combining into a more complex dynamic surface. Our protocol did not reproduce a surface with mixtures of ripples and breaking waves that would be common in open water and wind-exposed shorelines and would result in the largest degree of fragmentation and loss of image integrity through Snell's window.

Foraging success will vary with the visual processing capabilities of the predator (Katzir *et al.*, 1989; Lotem *et al.*, 1991) as well as that of subsurface prey. On average, one might expect that increased distortion of the profile of the forager through the interface will compromise or slow identification by the prey. For example, we observed that during low flow, the total area of the upright models was reduced relative to their crouched counterpart, potentially reducing their detection by subsurface prey. This difference may be informative in the foraging behaviour of heron-like predators as to their position in the window (i.e. upright vs. crouched), the former decreasing detectability by subsurface prey but also increasing linear distance from the prey. In addition, the extensive fragmentation we observed with increased flow may further limit identification of a predator. Yet fishes exhibit several adaptations to partially correct for the effect. For example, processing visual stimuli at a global rather than a local level and therefore interpreting all stimuli within the visual field as a complete set has been observed (Truppa *et al.*, 2010). Recognizing initial shape when parts of the shape are occluded has also been observed in fishes (Sovrano & Bisazza, 2007). This probably accounts for the ability of salmon to detect above-surface threats even when these are highly distorted or fragmented (Reimchen *et al.*, 2021). Differentiating individual 'frames' for rapidly changing model shapes with highly distorted dynamic surfaces will depend on flicker-fusion rates. Where these have been quantified in a broad range of terrestrial and aquatic taxa, including crustaceans and fish (Horodysky *et al.*, 2010; Rospars & Meyer-Vernet, 2021), most exhibit rates between 40 and 80 Hz, with instances up to 160 Hz (Kingston *et al.*, 2020), relative to human sensitivity (60 Hz), therefore indicating a capacity for differentiating these rapid changes through the fragmented optical window. This might contribute to results for multiple studies of avian piscivores (Dunn, 1973; Grubb, 1977; Bovino & Burtt, 1979; Taylor, 1983; Dodd & Colwell, 1996; McGowan *et al.*, 2002; Green & Leberg, 2005; Taylor & Taylor, 2005) that generally demonstrate reduction in capture success in windy conditions usually thought to be due to reduced detection of the subsurface prey. However, a recent study of terns (Laridae) found elevated foraging rates near upwellings and vortices due to higher fish densities (Lieber *et al.*, 2021).

Could our experimental results have relevance to frontal and ventral plumage variation in avian foragers that use the water–air interface? Given the emergence of birds in the Mesozoic, it is reasonable to assume that these have developed plumage adaptations to facilitate capture of prey that responded to visual cues. The white ventral plumage of many seabirds such as gulls and terns (Laridae) is known to increase capture success of surface fishes presumably as the white plumage compensates for shadow and is camouflaged against the sky background (Gotmark, 1987). The same process could also account for the white frontal plumage of some large waders (Ardeidae) and numerous shorebirds (Charadriidae) that forage in open and well-illuminated habitats, as the background against which the foragers are seen would tend to be largely sky rather than terrestrial (Green & Leberg, 2005). However, the majority of waders and shorebirds exhibit various combinations of speckled, mottled, streaked or barred frontal plumage (Sibley, 2014), much of which probably represents camouflage to aerial or terrestrial predators during nesting or foraging (Cott, 1940; Kushlan, 1976, 2009). Yet fragmentation of our uniformly coloured models when viewed through the optical window are comparable to patches and bars present on the frontal plumage of many species that forage in shallow water. Such disruptive patterns, when viewed against heterogeneous backgrounds, can decrease detectability by prey or predators (Cott, 1940; Schaefer & Stobbe, 2006; Stevens *et al.*, 2009) and this might be particularly important in shoreline habitats when foragers are positioned at the edge of the optical window and projected against a terrestrial background. Among the 68 species of herons and allies (Ardeidae), 52 exhibit variations in streaked and patch-marked plumage patterns (Fig. 5A) that are almost exclusively present along the ventral frontal portion

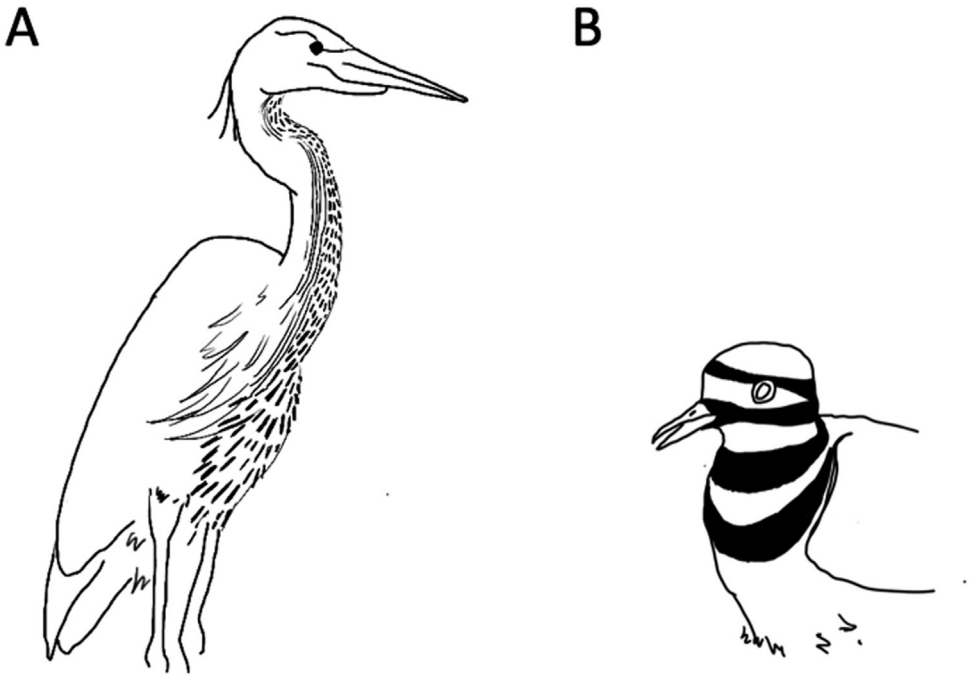

Figure 5. Stylized plumage patterns of great blue heron (*Ardea herodias*) and killdeer (*Charadrius vociferous*).

of the body (extracted from Billerman *et al*., 2022). We suggest that the fragmentation occurring through the optical window will provide a selective advantage for the evolution of these frontal plumage patterns.

We observed that with smooth waves, the profile of each model was fragmented by one or more horizontal bands (see Fig. 3.3, A–D and Supporting Information, Fig. S2). These bands result from shadowing by sequential waves blocking the transmission of above-surface light (Molkov, 2018) and which will define the profile of the forager through the window. This optically induced banding might favour development of distinctive plumage patterns. It is interesting to note that some shoreline birds, including killdeer, semipalmated plover, piping plover and ruddy turnstone, have distinctive dark horizontal bars rather than speckles on the frontal plumage (Fig. 5B). Other taxa such as stilt sandpiper and wandering tattler have combinations of horizontal ventral banding and frontal speckles and these may be reflective of a broader foraging niche.

The primary goal of this study was to quantify how differing water surface conditions affect above-surface image formation through Snell's window using a model that resembled a large avian wader (Ardeidae). We demonstrate a consistent and repeated relationship between the extent of banding and fragmentation of the models with water surface conditions. We suspect that this loss of shape integrity will generally benefit shoreline birds during foraging due to reduced detectability by the subsurface prey. If our study has a broader context, it suggests a complex interplay between foraging success and water surface conditions but also potential adaptive features in the emergence of different frontal plumage patterns of wading birds dependent on water surface conditions. Our experimental observations do not detract from the well-recognized benefit of disruptive patterns for camouflage against predators during nesting and foraging (Cott, 1940; Endler, 1992; Cuthill *et al*., 2017; Michalis *et al*., 2017; Billerman *et al*., 2022; for an alternative interpretation, see Somveille *et al*., 2016). However, profile distortion, fragmentation and banding of an above-surface object through Snell's window is an inevitable consequence of departures from flat water surfaces. We feel that this largely unexplored visual geometry between prey and predator, which is bi-directional (view from below vs. view from above), provides a rich avenue for studies of species using the water–air interface.

ACKNOWLEDGEMENTS

We thank Liana Zanette and Mike Clinchy for discussion and Sheila Douglas and an anonymous reviewer for comments on the manuscript. This work was supported by a Natural Sciences and Engineering

Research Council Operating grant to T.E.R. (NRC2354). We have no conflicts of interest to declare.

DATA AVAILABILITY

The data including R-code underlying this article will be shared on reasonable request to the corresponding author.

REFERENCES

Billerman SM, **Keeney BK**, **Rodewald PG**, **Schulenberg TS. 2022**. *Birds of the World*. Ithaca, NY: Cornell Laboratory of Ornithology. Available at: https://birdsoftheworld.org/bow/home

Bovino RR, **Burtt EH Jr**. **1979**. Weather-dependent foraging of great blue herons (*Ardea herodias*). *The Auk* **1**: 628–630.

Cott HB. 1940. *Adaptive coloration in animals*. London: Methuen.

Cuthill IC, **Allen WL**, **Arbuckle K**, **Caspers B**, **Chaplin G**, **Hauber ME**, **Hill GE**, **Jablonski NG**, **Jiggins CD**, **Kelber A**, **Mappes J**, **Marshall J**, **Merrill R**, **Osorio D**, **Prum R**, **Roberts NW**, **Roulin A**, **Rowland HM**, **Sherratt TN**, **Skelhorn J**, **Speed MP**, **Stevens M**, **Stoddard MC**, **Stuart-Fox D**, **Talas L**, **Tibbetts E**, **Caro T. 2017**. The biology of color. *Science* **357**: eaan0221.

Day RD, **Mueller F**, **Carseldine L**, **Meyers-Cherry N**, **Tibbetts IR. 2016**. Ballistic Beloniformes attacking through Snell's Window. *Journal of Fish Biology* **88**: 727–734.

Dill LM. 1977. Refraction and the spitting behavior of the archerfish (*Toxotes chatareus*). *Behavioral Ecology and Sociobiology* **2**: 169–184.

Dodd SL, **Colwell MA. 1996**. Seasonal variation in diurnal and nocturnal distributions of nonbreeding shorebirds at North Humboldt Bay, California. *The Condor* **98**: 196–207.

Dunn EK. 1973. Changes in fishing ability of terns associated with wind speed and sea surface conditions. *Nature* **244**: 520–521.

Endler JA. 1992. Signals, signal conditions and the direction of evolution. *The American Naturalist* **139**: S125–S153.

Gotmark F. 1987. White underparts in gulls function as hunting camouflage. *Animal Behaviour* **35**: 1786–1792.

Green MC, **Leberg PL. 2005**. Influence of plumage colour on prey response: does habitat alter heron crypsis to prey? *Animal Behaviour* **70**: 1203–1208.

Grubb TG Jr. **1977**. Weather-dependent foraging in Ospreys. *The Auk* **1**: 146–149.

Horodysky AZ, **Brill RW**, **Warrant EJ**, **Musick JA**, **Latour RJ. 2010**. Comparative visual function in four piscivorous fishes inhabiting Chesapeake Bay. *Journal of Experimental Biology* **213**: 1751–1761.

Horváth G, **Varjú D. 1995**. Underwater refraction-polarization patterns of skylight perceived by aquatic animals through Snell's window of the flat water surface. *Vision Research* **35**: 1651–1666.

Katzir G, **Lotem A**, **Intrator N. 1989**. Stationary underwater prey missed by reef herons, *Egretta gularis*: head position and light refraction at the moment of strike. *Journal of Comparative Physiology* **165**: 573–576.

Kingston AC, **Chappell DR**, **Speiser DI. 2020**. A snapping shrimp has the fastest vision of any aquatic animal. *Biology Letters* **16**: 20200298.

Klinka DR, **Reimchen TE. 2002**. Nocturnal and diurnal foraging behaviour of brown bears (*Ursus arctos*) on a salmon stream in coastal British Columbia. *Canadian Journal of Zoology* **80**: 1317–1322.

Klinka DR, **Reimchen TE. 2009**. Adaptive coat color polymorphism in the Kermode bear of coastal British Columbia. *Biological Journal of the Linnean Society* **98**: 479–488.

Kushlan JA. 1976. Feeding behaviour of North American herons. *Auk* **93**: 86–94.

Kushlan JA. 2009. Foraging and plumage coloration of the Galapagos Lava Heron (*Butorides striata sundevalli*). *Waterbirds* **32**: 415–422.

Lieber L, **Langrock R**, **Nimmo-Smith WA. 2021**. A bird's-eye view on turbulence: seabird foraging associations with evolving surface flow features. *Proceedings of the Royal Society B: Biological Sciences* **288**: 20210592.

Lotem A, **Schechtman E**, **Katzir G. 1991**. Capture of submerged prey by little egrets, *Egretta garzetta garzetta*: strike depth, strike angle and the problem of light refraction. *Animal Behaviour* **42**: 341–346.

Lynch DK. 2015. Snell's window in wavy water. *Applied Optics* **54**: B8–11.

Lythgoe JN. 1979. *The ecology of vision*. Oxford: Oxford University Press.

McGowan AN, **Cresswell WI**, **Ruxton GD. 2002**. The effects of daily weather variation on foraging and responsiveness to disturbance in overwintering red knot *Calidris canutus*. *Ardea* **90**: 229–237.

Michalis C, **Scott-Samuel NE**, **Gibson DP**, **Cuthill IC. 2017**. Optimal background matching camouflage. *Proceedings of the Royal Society B: Biological Sciences* **284**: 201707091858.

Molkov AA. 2018. The role of the effect of shadowing of some wavy regions by other wavy regions in the formation of an image of Snell's window. *Radiophysics and Quantum Electronics* **61**: 467–477.

Pau G, **Fuchs F**, **Sklyar O**, **Boutros M**, **Huber W. 2010**. EBImage – an R package for image processing with applications to cellular phenotypes. *Bioinformatics* **26**: 979–981.

R Core Team. 2022. *R: A language and environment for statistical computing*. R Foundation for Statistical Computing.

Reimchen TE. 2000. Some ecological and evolutionary aspects of bear–salmon interactions in coastal British Columbia. *Canadian Journal of Zoology* **78**: 448–457.

Reimchen TE, **Hunter D**, **Eggenberger JH. 2021**. Black bear colour polymorphism through a fragmented Snell's window. *Biological Journal of the Linnean Society* **134**: 1–10.

Rospars JP, **Meyer-Vernet N. 2021**. How fast do mobile organisms respond to stimuli? Response times from bacteria

to elephants to whales. *Physical Biology, Institute of Physics: Hybrid Open Access* **18**: ff10.1088/1478-3975/abcd88ff. ffhal-03171698f.

Schaefer HM, **Stobbe N. 2006**. Disruptive coloration provides camouflage independent of background matching. *Proceedings of the Royal Society B: Biological Sciences* **273**: 2427–2432.

Sibley DA. 2014. *The Sibley guide to birds*. New York: A. A. Knopf.

Somveille M, **Marshall KLA**, **Gluckman TL. 2016**. A global analysis of bird plumage patterns reveals no association between habitat and camouflage. *PeerJ* **4**: e2658.

Sovrano VA, **Bisazza A. 2007**. Recognition of partly occluded objects by fish. *Animal Cognition* **11**: 161–166.

Stevens M, **Winney IS**, **Cantor A**, **Graham J. 2009**. Outline and surface disruption in animal camouflage. *Proceedings of the Royal Society B: Biological Sciences* **276**: 781–786.

Taylor IR. 1983. Effect of wind on the foraging behaviour of Common and Sandwich Terns. *Ornis Scandinavica* **14**: 90–96.

Taylor IR, **Taylor SG. 2005**. The effect of wind on the foraging behaviour of Black-winged Stilts in SE Australia. *Wader Study Group Bull* **106**: 47–50.

Temple S, **Hart NS**, **Marshall NJ**, **Collin SP. 2010**. A spitting image: specializations in archerfish eyes for vision at the interface between air and water. *Proceedings of the Royal Society B: Biological Sciences* **277**: 2607–2615.

Truppa V, **Sovrano VA**, **Spinozzi G**, **Bisazza A. 2010**. Processing of visual hierarchical stimuli by fish (*Xenotoca eiseni*). *Behavioral Brain Research* **207**: 51–60.

Weller H. 2019. *countcolors: Locates and Counts Pixels Within Color Range(s) in Images. R package version 0.9.1*. Available at: https://CRAN.R-project.org/package=countcolors

Wickham H. 2016. *ggplot2: Elegant Graphics for Data Analysis*. New York: Springer.

SUPPORTING INFORMATION

Additional Supporting Information may be found in the online version of this article at the publisher's web-site.

Methods S1. Detailed characterization of the video sequences obtained and model appearance.
Methods S2. Detailed image analyses.
Video S1. Experimental formation of waves.
Video S2. Video used to derive frames of the crouched heron model through a wave surface.
Video S3. Video used to derive frames of the crouched heron model through low flow.
Video S4. Video used to derive frames of the crouched heron model through medium flow.
Video S5. Video used to derive frames of the crouched heron model through high flow.
Table S1. Central RGB vectors and respective radial values defined for each frame set (30 separate experimental conditions) used to target model pixels in each frame using the R-package 'countcolors'.
Figure S1. A visual representation of the steps carried out within the processing and analysis of images obtained from experimental videos. A, a representative frame capturing the CW model through the surface (Snell's window) under medium flow surface conditions. B, the equivalent frame after location of red model pixels and replacement with pure-black pixels in the first step of image analysis using countcolors (R-package: countcolors, Weller, 2019). C, the following step in image analysis where all background pixels were targeted and replaced with a uniformly yellow background. D, images were then converted to greyscale and underwent edge adjustments as shown in frame E before being analysed and quantified using EBImage (R-package EBImage, Pau *et al.*, 2010).
Figure S2. Visual representation of the temporal change in model appearance through wave, low flow, medium flow and high flow surface conditions. For each condition, six sequential frames (equivalent to 0.6 s in real time) obtained from videos at a rate of 10 frames per second are shown for each experimental model (TH, CH, TB, CB). Image frames have been cropped from their original size in which they were analysed (1920 × 1080 pixels) to dimensions of 1080 × 1080.